

Cite this: *J. Mater. Chem. A*, 2021, 9, 2734

Ferroelectricity in 2D metal phosphorus trichalcogenides and van der Waals heterostructures for photocatalytic water splitting†

Sheng Huang, Zhigang Shuai  and Dong Wang *

Integration of ferroelectricity into van der Waals heterostructures offers additional opportunities to control over the properties and functionalities of heterostructures by switching the direction of polarization via an external electric field. To discover potential ferroelectric monolayers that exhibit out-of-plane electric polarizations, we screen a family of metal phosphorus trichalcogenides $M_1M_2P_2X_6$ with $M_1 = \text{Cu/Ag}$, $M_2 = \text{In/Bi}$, $X = \text{S/Se}$ using density functional theory calculations. We predict room-temperature ferroelectricity in CuInP_2S_6 and CuBiP_2S_6 monolayers with out-of-plane polarizations (P_s) of $0.59 \mu\text{C cm}^{-2}$ and $0.35 \mu\text{C cm}^{-2}$, respectively. The strong metal-chalcogenide $M_1\text{-X}$ bond in the two Cu and S-based systems is responsible for their high phase transition temperatures. The polarizations in ferroelectric monolayers can persist in van der Waals heterostructures, and band gaps as well as band alignment of the heterostructures can be tuned by switching the polarization direction. Finally, we demonstrate that both visible light absorption and type-II band alignment facilitating fast charge separation can be realized in $\text{CuInP}_2\text{S}_6/\text{Mn}_2\text{P}_2\text{S}_6$ and $\text{CuInP}_2\text{S}_6/\text{Zn}_2\text{P}_2\text{Se}_6$ ferroelectric heterostructures, which are promising for applications in photocatalytic water splitting.

Received 1st October 2020
Accepted 14th December 2020

DOI: 10.1039/d0ta09618k

rsc.li/materials-a

1. Introduction

Ferroelectric materials with spontaneous electric polarizations switchable by an external electric field have been widely applied in non-volatile memories, field-effect transistors, sensors and other devices.^{1,2} A large variety of ferroelectric materials are ferroelectric perovskites with the ABX_3 type crystal structure, including BaTiO_3 , PbTiO_3 and emergent organic-inorganic as well as metal-free organic perovskites.³ A serious issue associated with ferroelectric perovskites is that their thin films often suffer from interactions with the substrate, which can damage their intrinsic spontaneous polarizations, making them difficult to integrate into nanoscale devices.⁴⁻⁶ As a contrast, van der Waals (vdW) crystals⁷⁻⁹ with intrinsic layered structures lack dangling bonds when exfoliated into thin layers and they interact weakly with the substrate, which turn them into ideal candidates for ultrathin ferroelectric applications.¹⁰

For materials to exhibit spontaneous electric polarizations, structures with no centrosymmetry in the polarization direction are a prerequisite. Room-temperature ferroelectricity in atomic thick layers is scarce, so far only a few ferroelectric monolayers have been reported experimentally, including the

in-plane polarization observed in single-layer SnS and SnTe ,^{11,12} the out-of-plane polarization in distorted 1T-MoTe_2 (ref. 13) and both in-plane and out-of-plane polarizations observed in $\alpha\text{-In}_2\text{Se}_3$.¹⁴ Meanwhile, theoretical calculations have predicted a bunch of two-dimensional (2D) ferroelectric materials including PbTe , SbN , BiP and single-element As , Sb , and Te monolayers.¹⁵⁻¹⁸ Most of them have in-plane polarizations, and only a few show out-of-plane polarizations such as 1T-MoS_2 , oxide graphene and Sc_2CO_2 .¹⁹⁻²¹ We noticed that interesting ferroelectric or anti-ferroelectric orderings were previously discovered in bulk metal phosphorus trichalcogenides (MPTs) that possess vdW layered structures.^{22,23} And thin-layered CuInP_2S_6 with about 20 nm thickness or even 4 nm thickness was shown to be ferroelectric at room temperature.^{24,25} Ferroelectric field-effect transistors based on CuInP_2S_6 and MoS_2 heterostructures and ferroelectric tunnel junctions using CuInP_2S_6 as the ferroelectric barrier have been fabricated, which work at room temperature and show a large on-off ratio.^{26,27} To discover atomic thick ferroelectric materials with out-of-plane polarizations, we screen the family of MPTs, including $M_1M_2P_2X_6$ with $M_1 = \text{Cu/Ag}$, $M_2 = \text{In/Bi}$, $X = \text{S/Se}$, using density functional theory (DFT) calculations, and unveil how elemental substitutions at the metal and chalcogenide sites affect the ferroelectricity of 2D MPTs. We predict that all of these MPTs are ferroelectric except for $\text{AgInP}_2\text{Se}_6$, but only two of them, CuInP_2S_6 and CuBiP_2S_6 , exhibit stable out-of-plane polarizations above room temperature. The ferroelectricity of CuInP_2S_6 and CuBiP_2S_6 monolayers is also

MOE Key Laboratory of Organic OptoElectronics and Molecular Engineering, Department of Chemistry, Tsinghua University, Beijing 100084, P. R. China. E-mail: dong913@tsinghua.edu.cn

† Electronic supplementary information (ESI) available. See DOI: 10.1039/d0ta09618k

investigated in the presence of domain walls, an external electric field and strain, which provides further evidence for the device potential of these 2D ferroelectric materials. Finally, we demonstrate that both the band gaps and band alignment of ferroelectric vdW heterostructures can be modulated by switching the direction of polarization *via* an electric field, and show that CuInP₂S₆/Mn₂P₂S₆ and CuInP₂S₆/Zn₂P₂Se₆ heterostructures with visible light absorption and type-II band alignment can be applied to photocatalytic water splitting.

2. Computational methods

All the calculations were performed by using the Vienna *Ab initio* Simulation Package (VASP version 5.4.1).²⁸ A vacuum layer of 25 Å was added in the out-of-plane direction to avoid interactions between periodic images. The projected augmented wave (PAW) method and Perdew–Burke–Ernzerhof (PBE) functional²⁹ within the generalized gradient approximation (GGA) were adopted. The cutoff energy of 600 eV for the plane-wave basis combined with Γ -centered k -mesh of $9 \times 9 \times 1$ was used in self-consistent calculations. The convergence criterion was 10^{-6} eV for the total energy, and 10^{-3} eV Å⁻¹ for forces during structural optimizations. To account for van der Waals interactions, Grimme's D3 dispersion correction³⁰ to the total energy was applied throughout the calculations. After structural optimizations with the PBE-D3 functional, a hybrid functional developed by Heyd, Scuseria and Ernzerhof (HSE06)³¹ was used in the electronic band structure and density of states (DOS) calculations for all the systems. To consider the on-site Coulomb interactions of transition metal Mn, the DFT+U method³² was applied with an effective U of 4 eV according to the literature³³ to optimize the structure of Mn₂P₂S₆ and CuInP₂S₆/Mn₂P₂S₆. Spin-polarized calculations were performed for all the systems, with an initial spin of $1\mu_B$ on each atom and $5\mu_B$ on Mn atom. The results show that all the MPTs are non-magnetic except for Mn₂P₂S₆ and heterostructures based on it.

To examine the stability of the monolayer ferroelectric structure, phonon spectra were obtained with the finite-displacement method by combining the VASP and Phonopy code.³⁴ The *ab initio* molecular dynamics simulations were carried out in a $4 \times 4 \times 1$ supercell at the Γ -point only. Ferroelectric polarizations were obtained using the Berry phase approach,³⁵ and both ionic and electronic contributions were taken into account. The energy barrier for the polarization reversal process was obtained with the nudged-elastic-band (NEB) method.³⁶ The external electric field in the out-of-plane direction was applied by inserting a dipole layer in the middle of the vacuum region. The LOBSTER code³⁷ was used to analyze the bond strength (pCOHP) and projected density-of-states (pDOS) based on the PAW calculations of solids.

3. Results and discussion

3.1 Structure of MPTs

Bulk metal phosphorus trichalcogenides adopt a hexagonal lamellar structure.³⁸ In each lamella of MPTs, metal atoms occupy 2/3 of the octahedral holes defined by the chalcogenide

framework, while P–P dimers occupy the remaining 1/3. Each S/Se atom is bonded to a single P atom and coordinated by two metal atoms, forming an MPX₃ type structure. The crystal structures of bulk MPTs were taken from the ICSD database (Table S1†). Bulk MPTs have weak interlayer vdW interactions; actually thin layered MPTs such as CuInP₂S₆ and CuCrP₂S₆ have been recently fabricated by mechanical exfoliation methods,^{25,39} and we expect a monolayer can be easily cleaved from the bulk. The cleavage energy of all eight MPTs was calculated and it is smaller than that of graphite,⁴⁰ manifesting the feasibility of fabricating single-layer and few-layer MPTs by exfoliations (Fig. S1†).

The optimized structures of single-layer MPTs are shown in Fig. 1a. All of them, except for AgInP₂Se₆, share similar structures with no centrosymmetry. Instead of locating at the

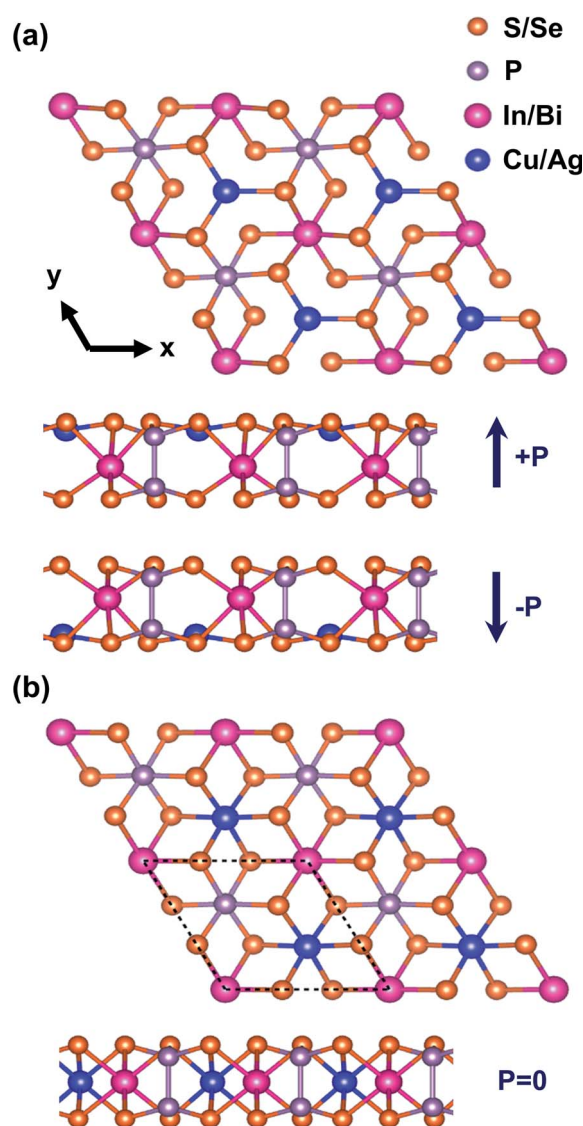


Fig. 1 Top and side views of single layer M1M2P₂X₆. (a) Non-centrosymmetric structure denoted as the ferroelectric phase structure. Two degenerate structures with opposite polarizations are shown. (b) Centrosymmetric structure denoted as the paraelectric phase structure. Black dashed lines represent a unit cell.

octahedral site, $M1 = \text{Cu/Ag}$ atoms shift predominantly in the out-of-plane direction. As a result of the large off-center shift of $M1$ atoms, three short metal-chalcogenide ($M1-X$) bonds and three long metal-chalcogenide ($M1-X$) bonds are formed, instead of six equivalent bonds. Meanwhile, there exists a smaller shift of $M2 = \text{In/Bi}$ atoms in the opposite direction. The dynamical stability of single-layer structures was confirmed by phonon spectra lack of imaginary frequencies and molecular dynamics simulations (Fig. S2†). The structural parameters of single-layer MPTs are summarized in Table S2,† in which Z_{M1} and Z_{M2} represent the off-center displacement of metal atoms in the out-of-plane direction. The shift of $M1$ in CuInP_2S_6 (1.37 Å) is larger than that in $\text{CuInP}_2\text{Se}_6$ (1.29 Å) and AgInP_2S_6 (1.17 Å), indicating that the shift in Cu and S-based systems is the largest. As a result, the polarization in CuInP_2S_6 is the largest among all MPTs.

Several previous theoretical studies predicted that single-layer CuInP_2S_6 and $\text{CuInP}_2\text{Se}_6$ are anti-ferroelectric based on PBE-D3 and PBE-D2 calculations.^{41–43} They also showed that in the presence of compressive strain or an electric field, the ground state of single-layer CuInP_2S_6 and $\text{CuInP}_2\text{Se}_6$ can be tuned to the ferroelectric state. To ascertain that the ferroelectric (FE) monolayers of MPTs can exist, we also calculated the energy of anti-ferroelectric (AFE) configuration in a $2 \times 1 \times 1$ supercell. It turned out that the ferroelectric structure is more stable than the anti-ferroelectric one in CuBiP_2S_6 , $\text{CuBiP}_2\text{Se}_6$, and all Ag-based MPTs. However the energy of anti-ferroelectric CuInP_2S_6 is 0.4 meV per formula unit lower than the ferroelectric one, and that of anti-ferroelectric CuInP_2S_6 is 23.6 meV lower (Table S3†). The energy of ferroelectric and anti-ferroelectric $\text{CuInP}_2\text{Se}_6$ is almost degenerate. Actually, both anti-ferroelectric and ferroelectric in-plane domains were recently observed in bulk CuInP_2S_6 .⁴⁴ We further calculated the transition energy path between anti-ferroelectric and ferroelectric structures in the absence of as well as in the presence of an electric field. Our results show that the minimum energy pathway between AFE and FE CuInP_2S_6 is 145.7 meV, much larger than the energy difference of 23.6 meV. And, applying an electric field of 0.35 V \AA^{-1} can turn the ground state of CuInP_2S_6 ferroelectric. The same result holds for monolayer $\text{CuInP}_2\text{Se}_6$

(78 meV energy switching barrier between AFE and FE states *versus* a 0.4 meV energy difference between them, as shown in Fig. S3†). As a result, it is possible to prepare the ferroelectric CuInP_2S_6 and $\text{CuInP}_2\text{Se}_6$ monolayers by the application of an electric field and the ferroelectric structures remain stable even after the electric field is removed. In the following, we will only discuss the ferroelectric MPT monolayers.

3.2 Ferroelectricity in single-layer MPTs

The off-center displacement of metal atoms breaks centrosymmetry, so the electric polarization in the out-of-plane direction arises. The polarization of single-layer $M1M2P_2X_6$ falls within a range of $0.35\text{--}0.59 \mu\text{C cm}^{-2}$ (Table 1) by assuming an effective thickness of 6.5 Å for the monolayer. The polarization in single-layer CuInP_2S_6 is the largest, and it is two orders-of-magnitude lower than that in prototypical bulk ferroelectric BaTiO_3 ($\sim 26 \mu\text{C cm}^{-2}$). The small polarizations in MPTs mainly arise from displacements of metal atoms $M1$ and $M2$ in opposite directions, whose contributions to overall polarization cancel out to some extent, forming the so-called ‘ferrielectric’ pattern.

Below we take two Cu and S-based systems, CuInP_2S_6 and CuBiP_2S_6 as examples, to unravel the polarization reversal behavior of 2D MPTs. Firstly, minimal energy pathway (MEP) mapping between two stable ferroelectric phase structures with opposite polarizations is constructed by the nudged-elastic-band (NEB) method. As shown in Fig. 1b and 2a, the high-energy structure is centrosymmetric with all metal atoms located at the octahedral center, which represents the paraelectric structure. A typical ferroelectric–paraelectric–ferroelectric transition pathway is identified, with an activation barrier of 335 meV per unit cell in CuInP_2S_6 and 326 meV in CuBiP_2S_6 . Along the structural phase transition path, metal atoms exhibit large off-center displacement perpendicular to the atomic plane, resulting in the polarization of $0.59 \mu\text{C cm}^{-2}$ in CuInP_2S_6 and $0.35 \mu\text{C cm}^{-2}$ in CuBiP_2S_6 (Fig. 2b). Subsequently, *ab initio* molecular dynamics simulations at temperatures between 50 K and 800 K were performed. Taking the out-of-plane z -coordinate difference between metal atoms $M1$ and $M2$ ($Z_{M1} - Z_{M2}$) as the

Table 1 Ferroelectric structures and properties of single-layer MPTs. Z_{M1} ($M1 = \text{Cu/Ag}$) and Z_{M2} ($M2 = \text{In/Bi}$): shift of metal atoms from the symmetry center in the out-of-plane direction; P_s : electric polarization; E_b : polarization switching barrier; T_C : phase transition temperature. The last two columns are the length and integrated projected crystal orbital Hamilton population (IpCOHP) of the $M1-X$ bond ($M1 = \text{Cu/Ag}$, $X = \text{S/Se}$)

System	$Z_{M1} - Z_{M2}$ (Å)	P_s ($\mu\text{C cm}^{-2}$)	E_b (meV)	T_C (K)	Length of $M1-X$ (Å)	IpCOHP of $M1-X$ (eV)
CuInP_2S_6	1.63	0.59	335	486	2.23	−5.77
CuBiP_2S_6	1.62	0.35	326	394	2.25	−5.95
$\text{CuInP}_2\text{Se}_6$	1.57	0.44	166	254	2.36	−5.57
$\text{CuBiP}_2\text{Se}_6$	1.56	0.39	160	194	2.38	−5.71
AgInP_2S_6	1.45	0.46	31	143	2.48	−4.66
AgBiP_2S_6	1.54	0.35	62	268	2.51	−4.86
$\text{AgInP}_2\text{Se}_6^a$	—	—	—	—	2.89	−4.40
$\text{AgBiP}_2\text{Se}_6^b$	1.38	0.34	25	—	2.64	−4.81

^a Monolayer $\text{AgInP}_2\text{Se}_6$ adopts a stable centrosymmetric structure without off-center displacement of metal atoms and ferroelectricity. ^b Monolayer $\text{AgBiP}_2\text{Se}_6$ doesn't show first-order transition with an obvious transition temperature (see Fig. S4c).

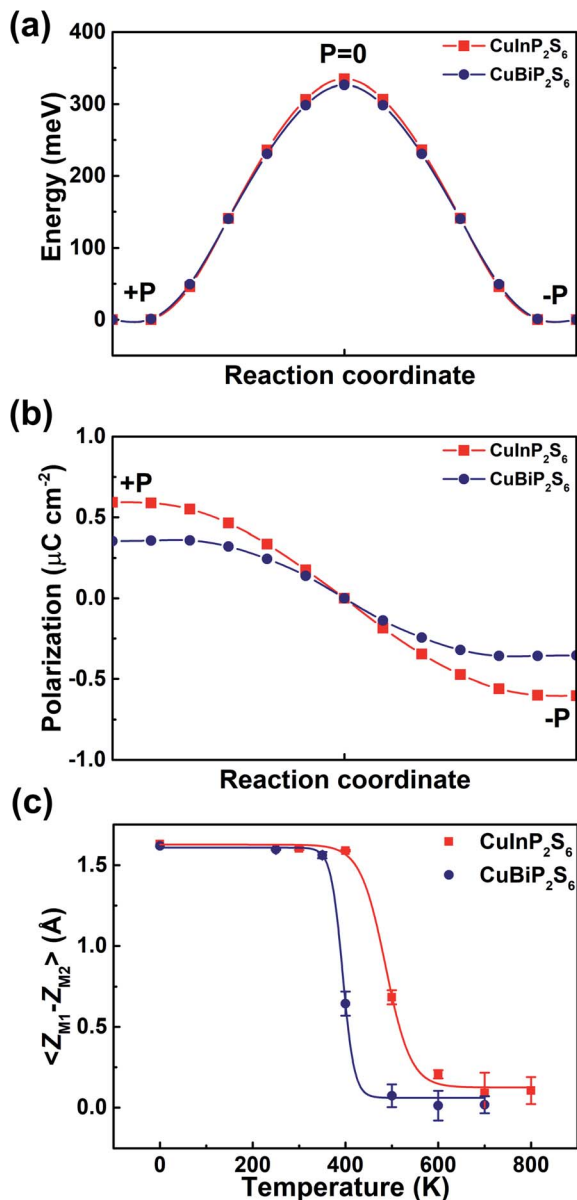


Fig. 2 Ferroelectric properties of single-layer CuInP_2S_6 and CuBiP_2S_6 . (a) Minimal energy pathway of the FE-PE-FE transition. (b) Polarization reversal along the pathway. (c) Statistical average of $Z_{M1} - Z_{M2}$ changing with the temperature from *ab initio* molecular dynamics simulations. The error bars of the data are given. The phase transition temperature T_C is obtained by a sigmoid fitting of the data.

order parameter, its time evolution clearly shows that single-layer ferroelectric CuInP_2S_6 and CuBiP_2S_6 can maintain their polarizations at temperatures up to 350 K, while at further higher temperatures polarizations diminish gradually, which is manifested by the disordered positions of Cu metal atoms. The statistical average of $Z_{M1} - Z_{M2}$ as a function of the temperature demonstrates phase transition to occur at T_C of 486 K and 394 K (Fig. 2c and Table 1), suggesting stable ferroelectricity in these Cu and S-based MPTs against room temperature. The results of other MPTs are provided in Fig. S4 and S5,[†] which show lower T_C in Ag and Se-based systems (Table 1).

The above results are based on MPTs with an ideal ferroelectric structure of infinite size. In experiment, domain walls between oppositely polarized states were observed in thin-layered CuInP_2S_6 .¹⁸ To explore the polarization reversal process in the presence of domain walls, we built an ideal ferroelectric structure ($\uparrow\uparrow\uparrow\uparrow$) and two possible domain wall structures ($\uparrow\uparrow\uparrow\downarrow$ and $\uparrow\uparrow\downarrow\downarrow$) in a $4 \times 1 \times 1$ supercell (Fig. S6a[†]). The energy of domain wall structures is very close to that of the ideal ferroelectric structure, indicating that these domain walls are easy to form. A similar MEP mapping between two degenerate ferroelectric states ($\uparrow\uparrow\uparrow\uparrow$ and $\downarrow\downarrow\downarrow\downarrow$) through domain wall structures ($\uparrow\uparrow\uparrow\downarrow$ and $\uparrow\uparrow\downarrow\downarrow$) has been calculated (Fig. S6b[†]). It shows that the energy barrier for polarization reversal is substantially lowered in the presence of domain walls. In CuInP_2S_6 , it decreases from 335 meV per unit cell to 70 meV per unit cell in the transition from the $\uparrow\uparrow\uparrow\uparrow$ to $\uparrow\uparrow\uparrow\downarrow$ state, and 73 meV per unit cell in the transition from the $\uparrow\uparrow\uparrow\downarrow$ to $\uparrow\uparrow\downarrow\downarrow$ state. These results manifest that the presence of domain walls between oppositely polarized domains actually facilitates the reversal of electric polarization along the kinetic pathway.

3.3 Ferroelectricity modulated by an electric field and strain

The electric polarization of ferroelectric materials can be reversed by the application of an external electric field. After an electric field is applied in the out-of-plane direction, the two oppositely polarized ferroelectric states are no longer degenerate. Their energy difference increases linearly with the electric field, as shown in Fig. S7,[†] so the population difference increases exponentially with the electric field. Meanwhile, the activation barrier decreases linearly with the electric field. At an electric field of 0.3 V \AA^{-1} , the energy difference between the two oppositely polarized ferroelectric states of CuInP_2S_6 is as large as 47 meV per unit cell and the activation barrier is lowered by 26 meV per unit cell. On the other hand, ferroelectric materials are also piezoelectric, which means ferroelectricity can be tuned by the application of strain. We show that after a uniaxial strain is applied along the in-plane x direction, both the activation barrier and the electric polarization are modulated to some extent. The activation barrier decreases in the presence of a compressive strain (Fig. S7[†]). The polarization decreases too, but the variation in the polarization is less dramatic than that in the activation barrier. An opposite trend has been observed when a tensile strain is applied. We attribute the decreased polarization with the application of the compressive strain to the decreased distance between M1 and M2 atoms, $Z_{M1} - Z_{M2}$, and the increased polarization with the tensile strain to the increased distance between M1 and M2.

3.4 Elemental substitution effect on the ferroelectricity of 2D MPTs

The ferroelectric properties of all single-layer MPTs, $\text{M1M2P}_2\text{X}_6$ with $\text{M1} = \text{Cu/Ag}$, $\text{M2} = \text{In/Bi}$, $\text{X} = \text{S/Se}$ have been shown in Table 1. Among them, CuInP_2S_6 and CuBiP_2S_6 exhibit the highest Curie temperature above 300 K and the highest energy barrier of polarization reversal (>300 meV per unit cell), while

CuInP₂Se₆ and CuBiP₂Se₆ exhibit the Curie temperature around 200 K and a moderate energy barrier (~160 meV). Ag-based systems have the lowest energy barrier (<100 meV). Clearly, elemental substitutions at the M1 metal site and X chalcogenide site significantly affect their polarization stability, while that at the M2 metal site has a marginal effect. Overall, we found superior ferroelectricity in Cu and S-based systems compared to Ag and Se-based ones.

To explain the substitution effect on the ferroelectricity of MPTs, we analyzed the partial density-of-states (pDOS) and projected crystal orbital Hamilton population (pCOHP) (Fig. 3) of both ferroelectric and paraelectric phase structures. pCOHP analysis can decompose energy of an electronic state in extended systems into contributions from chemical bonds. The negative and positive values of pCOHP indicate bonding and anti-bonding features of a certain bond, respectively. In the paraelectric phase of all single-layer MPTs, the valence band is featured predominantly by the metal-chalcogenide M1–X anti-bond while the conduction band is featured by the M2–X anti-bond. In the ferroelectric phase, a significant change is identified near the Fermi level (0 eV): accompanying the ferroelectric distortion and off-center displacement of M1, the anti-bonding feature of M1–X bond is remarkably diminished. The reduction of M1–X anti-bonding strength is observed in all ferroelectric MPTs (Fig. S8[†]), so we conclude that the M1–X (Cu/Ag–S/Se) bond plays a key role in stabilizing the ferroelectric structure. Since Cu and Ag atoms, as well as S and Se atoms are in the same group in the periodic table, and the atomic radius of Cu is smaller than that of Ag, and the atomic radius of S is smaller than that of Se, the Cu–S bond is shorter than the Cu–Se, Ag–S and Ag–Se bonds as shown in Table 1, which leads to a more stable ferroelectric structure in Cu and S-based MPTs. Indeed,

integrated pCOHP (IpCOHP) of the M1–X bond over the entire energy range below the Fermi level shows that IpCOHP of the Cu–S bond is most negative, which implies that the Cu–S bond is the strongest, followed by Cu–Se, Ag–S and Ag–Se. The strength of the M1–X bond correlates positively with the ferroelectric stability of M1M₂P₂S₆. In contrast, the M2 (In/Bi) metal atom contributes little to the DOS near the Fermi level (Fig. 3), so substitution at the M2 site has little effect on the ferroelectric stability, but substitution of In with Bi does affect the magnitude of electric polarization.

3.5 Ferroelectricity in vdW heterostructures

Finally, we demonstrate the device potential of 2D ferroelectric MPTs. A bilayer vdW heterostructure is constructed by stacking a monolayer of Zn₂P₂Se₆ or Mn₂P₂Se₆ on top of a monolayer of CuInP₂S₆ which is in the polarization state +P or –P (Fig. 4a). We use these two examples to show the tunable electronic properties of ferroelectric heterostructures by means of polarization reversal. Both Zn₂P₂Se₆ and Mn₂P₂Se₆ monolayers are non-ferroelectric and they show little lattice mismatch with CuInP₂S₆ (see Methods in the ESI[†]). The MEP mapping between +P and –P states in the CuInP₂S₆/Zn₂P₂Se₆ heterostructure shows that the activation barrier is 438 meV from the +P to –P state and 342 meV from the –P to +P state (Fig. 4b). However the activation barrier in the CuInP₂S₆/Mn₂P₂Se₆ heterostructure is 389 meV from the +P to –P and 299 meV from the –P to +P state. In both heterostructures, +P and –P states are no longer degenerate, due to the interlayer interactions. The activation barriers of polarization reversal are almost the same as those in the ferroelectric monolayer of CuInP₂S₆, indicating that the room-temperature ferroelectricity of CuInP₂S₆ can be retained in vdW heterostructures. As other MPTs, single-layer CuInP₂S₆ is a semiconductor with an indirect band gap of 2.79 eV. Due to the presence of an intrinsic dipole in the monolayer, the vacuum energy at the opposite sides of CuInP₂S₆ differs by 0.50 eV (Fig. S9[†]). After the direction of polarization is reversed by the external electric field, the band offset between Zn₂P₂Se₆ and CuInP₂S₆ monolayers will be shifted by 0.42 eV (which is close to the vacuum energy difference), and the band gap of the heterostructure is reduced from 1.98 eV in the +P state to 1.56 eV in the –P state (Fig. 4c and d). In both cases, the band alignment is of type-II with the valence band maximum (VBM) from Zn₂P₂Se₆ and the conduction band minimum (CBM) from CuInP₂S₆. However in the CuInP₂S₆/Mn₂P₂Se₆ heterostructure, both the CBM and the VBM are from CuInP₂S₆ in the +P state, giving rise to the type-I band alignment and a band gap of 2.86 eV close to that in monolayer CuInP₂S₆. When CuInP₂S₆ is in the –P state, the band alignment is of type-II with the VBM from Mn₂P₂Se₆ (only 0.06 eV higher than that of CuInP₂S₆) and the band gap is 2.73 eV (Fig. 4e and f). Ferroelectric heterostructures based on CuInP₂S₆ and g-C₃N₄ have been reported, which display substantially accelerated charge transfer and an enhanced photocatalytic H₂ evolution rate over paraelectric-phase CuInP₂S₆.⁴⁵ Theoretical studies also showed the potential of MPTs to be applied in photocatalytic water-splitting.^{10,46,47} To demonstrate the potential of these ferroelectric

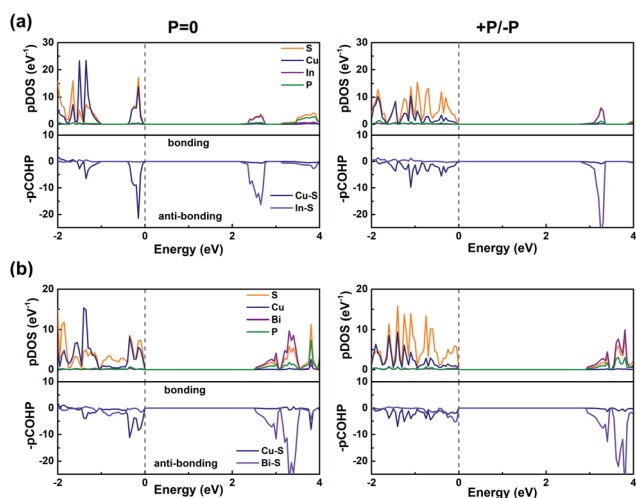


Fig. 3 Projected density-of-states (pDOS) and projected crystal orbital Hamilton population (pCOHP) analysis of paraelectric and ferroelectric MPTs. The dashed line denotes the Fermi level position. (a) CuInP₂S₆. (b) CuBiP₂S₆. Negative pCOHP values imply the bonding feature and positive ones imply the anti-bonding feature of a certain bond. These data show that the Cu–S bond plays a significant role in stabilizing the ferroelectric structure.

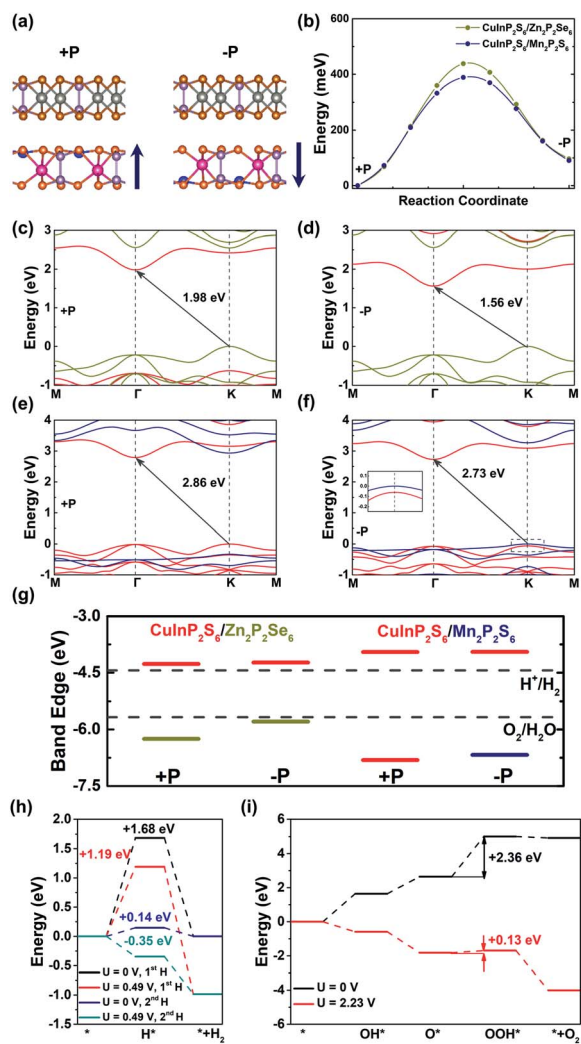


Fig. 4 CuInP₂S₆-based vdW heterostructures. (a) Side view of CuInP₂S₆-based heterostructures with CuInP₂S₆ in two oppositely polarized states, +P and -P. (b) Minimal energy pathway of the FE(+P)–FE(-P) transition. The +P and -P states are no longer degenerate in heterostructures. (c) Band structure of CuInP₂S₆/Zn₂P₂Se₆ with CuInP₂S₆ in the +P state. (d) Band structure of CuInP₂S₆/Zn₂P₂Se₆ with CuInP₂S₆ in the -P state. (e) Band structure of CuInP₂S₆/Mn₂P₂S₆ with CuInP₂S₆ in the +P state. (f) Band structure of CuInP₂S₆/Mn₂P₂S₆ with CuInP₂S₆ in the -P state. The electronic bands originating from CuInP₂S₆ are highlighted in red, those from Zn₂P₂Se₆ are in yellow and those from Mn₂P₂S₆ are in blue. (g) Band edge energies of all four heterostructures. The absolute potentials of the standard hydrogen electrode and oxygen electrode are shown for comparison. Free energy diagrams of the (h) HER and (i) OER on CuInP₂S₆/Mn₂P₂S₆ with CuInP₂S₆ in the -P state at pH = 0. $U = 0.49$ V and $U = 2.23$ V are the potentials caused by the photoexcitation for the HER and OER, respectively.

heterostructures for water splitting, the absolute band energy is obtained. Both heterostructures in both P+ and P- states show a valence band energy lower than the redox potential of O₂/H₂O (-5.67 eV) and the conduction band energy higher than the redox potential of H⁺/H₂ (-4.44 eV), indicating their potential abilities of photocatalytic water-splitting. By switching the ferroelectric polarization, the band gap in the CuInP₂S₆/

Zn₂P₂Se₆ heterostructure is tuned by 0.42 eV to the near-infrared region, while the band alignment in CuInP₂S₆/Mn₂P₂S₆ is tuned from type-I to type-II, which can promote electron and hole separation.

DFT methods have been widely applied to reveal the photocatalytic activity of 2D materials, including 2D ferroelectric materials.^{48–52} To show the catalytic activity of the ferroelectric heterostructure for water splitting, we calculated the free energy change of the HER and OER on CuInP₂S₆/Mn₂P₂S₆ with CuInP₂S₆ in the -P state. In photocatalytic water splitting, the potential of photogenerated electrons for the HER (U_e) arises from the energy difference between the CBM and the absolute potential of the hydrogen electrode, while that of photogenerated holes for the OER (U_h) is taken as the energy difference between the absolute potential of the hydrogen electrode and the VBM. At pH = 0, U_e and U_h of CuInP₂S₆ (-P)/Mn₂P₂S₆ are 0.49 eV and 2.23 eV, respectively. More computational details can be found in Table S4 and Methods in the ESI.† As shown in Fig. 4h for the HER, the free energy change of the first electron transfer step to form the H* intermediate is 1.68 eV. At the potential generated by photoexcitation ($U_e = 0.49$ eV), it is reduced to 1.19 eV, but still too high to activate the HER. However, when we consider a higher hydrogen coverage on the photocatalyst, such as the catalyst with one hydrogen already adsorbed to it as shown in Fig. S10,† the free energy change for the H* formation step is significantly reduced to 0.14 eV and the HER becomes energetically downhill with the help of photogenerated electrons ($U_e = 0.49$ eV). The OER follows a four-proton and four-electron pathway with the intermediates OH*, O*, and OOH*. The free energy profile for the OER on CuInP₂S₆ (-P)/Mn₂P₂S₆ is shown in Fig. 4i. The third step in which O* is oxidized to OOH* is the rate-limiting step since the free energy change in this step is the highest. At the potential produced by photoexcitation ($U_h = 2.23$ eV), the free energy change of this step has been reduced to 0.13 eV. We further analysed the pH effect on the HER and OER processes catalysed by CuInP₂S₆ (-P)/Mn₂P₂S₆. As we can see from Fig. S11,† with the help of photogenerated electrons and holes, both the HER and OER are energetically downhill at pH = 3. Based on these calculations, we conclude that the CuInP₂S₆ (-P)/Mn₂P₂S₆ ferroelectric heterostructure with type-II band alignment could be a promising photocatalyst for the water splitting process. In addition to photovoltaic and photocatalytic applications, ferroelectric vdW heterostructures also offer unique opportunities for realizing ultrathin non-volatile memories, field-effect transistors and other ferroelectric devices with new functionalities.

4. Conclusions

To summarize, we report two room-temperature 2D ferroelectric materials, CuInP₂S₆ and CuBiP₂S₆, discovered in the family of metal phosphorus trichalcogenides M1M2P₂X₆ with M1 = Cu/Ag, M2 = In/Bi, X = S/Se. Both phonon dispersion calculations and first-principles molecular dynamics simulations confirm that MPTs can be mechanically exfoliated down to a single layer. All of them, except for AgInP₂Se₆, exhibit ferroelectric

polarizations in the out-of-plane direction. The ferroelectric properties of Cu and S-based MPTs are superior to those of Ag and Se-based ones, because of the strong metal-chalcogenide bond M1–X, which plays an essential role in stabilizing the ferroelectric phase structure. CuInP₂S₆ and CuBiP₂S₆ monolayers exhibit a Curie temperature, T_C of 486 K and 394 K, and the electric polarization, P_s of 0.59 $\mu\text{C cm}^{-2}$ and 0.35 $\mu\text{C cm}^{-2}$, respectively. Room-temperature ferroelectricity of MPT monolayers can be well retained in vdW heterostructures constructed based on them. We demonstrate that these ferroelectric heterostructures are promising for photocatalytic water splitting, as well as for application in ultrathin nonvolatile memories, field effect transistors, and other ferroelectric devices of broad interest.

Conflicts of interest

There are no conflicts to declare.

Acknowledgements

This work was supported by the National Natural Science Foundation of China (Grant No. 21673123) and the Ministry of Science and Technology of China (Grant No. 2015CB655002). Computational resources were provided by the Tsinghua Supercomputing Center and National Computing Grid.

Notes and references

- J. F. Scott, *Science*, 2007, **315**, 954–959.
- L. W. Martin and A. M. Rappe, *Nat. Rev. Mater.*, 2017, **2**, 16087.
- H. Y. Ye, Y. Y. Tang, P. F. Li, W. Q. Liao, J. X. Gao, X. N. Hua, H. Cai, P. P. Shi, Y. M. You and R. G. Xiong, *Science*, 2018, **361**, 151–155.
- D. D. Fong, G. B. Stephenson, S. K. Streiffer, J. A. Eastman, O. Auciello, P. H. Fuoss and C. Thompson, *Science*, 2004, **304**, 1650–1653.
- J. Junquera and P. Ghosez, *Nature*, 2003, **422**, 506–509.
- C. H. Ahn, K. M. Rabe and J. M. Triscone, *Science*, 2004, **303**, 488–491.
- M. H. Wu and P. Jena, *Wiley Interdiscip. Rev.: Comput. Mol. Sci.*, 2018, **8**, e1365.
- C. J. Cui, F. Xue, W. J. Hu and L. J. Li, *npj 2D Mater. Appl.*, 2018, **2**, 18.
- Z. Guan, H. Hu, X. W. Shen, P. H. Xiang, N. Zhong, J. H. Chu and C. G. Duan, *Adv. Electron. Mater.*, 2019, **6**, 1900818.
- J. Shang, X. Tang and L. Z. Kou, *Wiley Interdiscip. Rev.: Comput. Mol. Sci.*, 2020, e1496.
- K. Chang, J. W. Liu, H. C. Lin, N. Wang, K. Zhao, A. M. Zhang, F. Jin, Y. Zhong, X. P. Hu, W. H. Duan, Q. M. Zhang, L. Fu, Q. K. Xue, X. Chen and S. H. Ji, *Science*, 2016, **353**, 274–278.
- N. Higashitarumizu, H. Kawamoto, C. J. Lee, B. H. Lin, F. H. Chu, I. Yonemori, T. Nishimura, K. Wakabayashi, W. H. Chang and K. Nagashio, *Nat. Commun.*, 2020, **11**, 2428.
- S. G. Yuan, X. Luo, H. L. Chan, C. C. Xiao, Y. W. Dai, M. H. Xie and J. H. Hao, *Nat. Commun.*, 2019, **10**, 1775.
- F. Xue, W. J. Hu, K. C. Lee, L. S. Lu, J. W. Zhang, H. L. Tang, A. Han, W. T. Hsu, S. B. Tu, W. H. Chang, C. H. Lien, J. H. He, Z. D. Zhang, L. J. Li and X. X. Zhang, *Adv. Funct. Mater.*, 2018, **28**, 1803738.
- X. L. Zhang, Z. X. Yang and Y. Chen, *J. Appl. Phys.*, 2017, **122**, 064101.
- C. Liu, W. H. Wan, J. Ma, W. Guo and Y. G. Yao, *Nanoscale*, 2018, **10**, 7984–7990.
- Y. Wang, C. C. Xiao, M. G. Chen, C. Q. Hu, J. D. Zou, C. Wu, J. Z. Jiang, S. Y. A. Yang, Y. H. Lu and W. Ji, *Mater. Horiz.*, 2018, **5**, 521–528.
- C. C. Xiao, F. Wang, S. Y. A. Yang, Y. H. Lu, Y. P. Feng and S. B. Zhang, *Adv. Funct. Mater.*, 2018, **28**, 1707383.
- S. N. Shirodkar and U. V. Waghmare, *Phys. Rev. Lett.*, 2014, **112**, 157601.
- A. Chandrasekaran, A. Mishra and A. K. Singh, *Nano Lett.*, 2017, **17**, 3290–3296.
- M. Noor-A-Alam and Y. H. Shin, *Phys. Chem. Chem. Phys.*, 2016, **18**, 20443–20449.
- M. A. Susner, M. Chyasnovichyus, M. A. McGuire, P. Ganesh and P. Maksymovych, *Adv. Mater.*, 2017, **29**, 1602852.
- F. M. Wang, T. A. Shifa, P. Yu, P. He, Y. Liu, F. Wang, Z. X. Wang, X. Y. Zhan, X. D. Lou, F. Xia and J. He, *Adv. Funct. Mater.*, 2018, **28**, 1802151.
- M. Chyasnovichyus, M. A. Susner, A. V. Ievlev, E. A. Eliseev, S. V. Kalinin, N. Balke, A. N. Morozovska, M. A. McGuire and P. Maksymovych, *Appl. Phys. Lett.*, 2016, **109**, 172901.
- F. C. Liu, L. You, K. L. Seyler, X. B. Li, P. Yu, J. H. Lin, X. W. Wang, J. D. Zhou, H. Wang, H. Y. He, S. T. Pantelides, W. Zhou, P. Sharma, X. D. Xu, P. M. Ajayan, J. L. Wang and Z. Liu, *Nat. Commun.*, 2016, **7**, 12357.
- J. B. Wu, H. Y. Chen, N. Yang, J. Cao, X. D. Yan, F. X. Liu, Q. B. Sun, X. Ling, J. Guo and H. Wang, *Nat. Electron.*, 2020, **3**, 466–472.
- M. W. Si, P. Y. Liao, G. Qiu, Y. Q. Duan and P. D. D. Ye, *ACS Nano*, 2018, **12**, 6700–6705.
- G. Kresse and J. Furthmüller, *Phys. Rev. B: Condens. Matter Mater. Phys.*, 1996, **54**, 11169–11186.
- J. P. Perdew, K. Burke and M. Ernzerhof, *Phys. Rev. Lett.*, 1996, **77**, 3865–3868.
- S. Grimme, J. Antony, S. Ehrlich and H. Krieg, *J. Chem. Phys.*, 2010, **132**, 154104.
- J. Heyd, G. E. Scuseria and M. Ernzerhof, *J. Chem. Phys.*, 2003, **118**, 8207–8215.
- S. L. Dudarev, G. A. Botton, S. Y. Savrasov, C. J. Humphreys and A. P. Sutton, *Phys. Rev. B: Condens. Matter Mater. Phys.*, 1998, **57**, 1505–1509.
- B. L. Chittari, Y. Park, D. Lee, M. Han, A. H. MacDonald, E. Hwang and J. Jung, *Phys. Rev. B*, 2016, **94**, 184428.
- A. Togo and I. Tanaka, *Scr. Mater.*, 2015, **108**, 1–5.
- R. D. Kingsmith and D. Vanderbilt, *Phys. Rev. B: Condens. Matter Mater. Phys.*, 1993, **47**, 1651–1654.
- G. Henkelman and H. Jonsson, *J. Chem. Phys.*, 2000, **113**, 9978–9985.

- 37 S. Maintz, V. L. Deringer, A. L. Tchougreff and R. Dronskowski, *J. Comput. Chem.*, 2016, **37**, 1030–1035.
- 38 V. Maisonneuve, V. B. Cajipe, A. Simon, R. VonDerMuhll and J. Ravez, *Phys. Rev. B: Condens. Matter Mater. Phys.*, 1997, **56**, 10860–10868.
- 39 Y. F. Lai, Z. G. Song, Y. Wan, M. Z. Xue, C. S. Wang, Y. Ye, L. Dai, Z. D. Zhang, W. Y. Yang, H. L. Du and J. B. Yang, *Nanoscale*, 2019, **11**, 5163–5170.
- 40 K. S. Novoselov, A. K. Geim, S. V. Morozov, D. Jiang, Y. Zhang, S. V. Dubonos, I. V. Grigorieva and A. A. Firsov, *Science*, 2004, **306**, 666–669.
- 41 Z. Z. Sun, W. Xun, L. Jiang, J. L. Zhong and Y. Z. Wu, *J. Phys. D: Appl. Phys.*, 2019, **52**, 465302.
- 42 S. A. Tawfik, J. R. Reimers, C. Stampfl and M. J. Ford, *J. Phys. Chem. C*, 2018, **122**, 22675–22687.
- 43 W. S. Song, R. X. Fei and L. Yang, *Phys. Rev. B*, 2017, **96**, 235420.
- 44 A. Dziaugys, K. Kelley, J. A. Brehm, L. Tao, A. Puretzky, T. L. Feng, A. O'Hara, S. Neumayer, M. Chyasnovichyus, E. A. Eliseev, J. Banys, Y. Vysochanskii, F. Ye, B. C. Chakoumakos, M. A. Susner, M. A. McGuire, S. V. Kalinin, P. Ganesh, N. Balke, S. T. Pantelides, A. N. Morozovska and P. Maksymovych, *Nat. Commun.*, 2020, **11**, 1–7.
- 45 B. Lin, A. Chaturvedi, J. Di, L. You, C. Lai, R. Duan, J. Zhou, B. Xu, Z. Chen, P. Song, J. Peng, B. Ma, H. Liu, P. Meng, G. Yang, H. Zhang, Z. Liu and F. Liu, *Nano Energy*, 2020, **76**, 104972.
- 46 C. F. Du, Q. H. Liang, R. Dangol, J. Zhao, H. Ren, S. Madhavi and Q. Y. Yan, *Nano-Micro Lett.*, 2018, **10**, 67.
- 47 X. Zhang, X. D. Zhao, D. H. Wu, Y. Jing and Z. Zhou, *Adv. Sci.*, 2016, **3**, 1600062.
- 48 L. Ju, J. Shang, X. Tang and L. Z. Kou, *J. Am. Chem. Soc.*, 2020, **142**, 1492–1500.
- 49 M. Qiao, J. Liu, Y. Wang, Y. F. Li and Z. F. Chen, *J. Am. Chem. Soc.*, 2018, **140**, 12256–12262.
- 50 C. F. Fu, J. Y. Sun, Q. Q. Luo, X. X. Li, W. Hu and J. L. Yang, *Nano Lett.*, 2018, **18**, 6312–6317.
- 51 Y. G. Li, Y. L. Li, B. S. Sa and R. Ahuja, *Catal. Sci. Technol.*, 2017, **7**, 545–559.
- 52 B. H. Jing, Z. M. Ao, W. N. Zhao, Y. Xu, Z. F. Chen and T. C. An, *J. Mater. Chem. A*, 2020, **8**, 20363–20372.